Tests of the Hydrodynamic Equivalence of Direct-Drive Implosions with Different D_2 and ^{3}He Mixtures

Introduction

Ignition and high gain in inertial confinement fusion (ICF)[1–3] requires an understanding of how the choice of materials affects implosion dynamics. ICF ignition targets are typically spherical capsules with an outer shell made of plastic or beryllium, a cryogenic layer of deuterium–tritium (DT) ice, and gaseous DT at the center. The direct-drive approach to ICF[4] implodes the target by direct illumination using multiple laser beams. Laser ablation of the capsule's outer surface drives the remaining payload inward, compressing and heating it to a state where nuclear fusion can occur.

Surrogate materials or configurations provide a convenient test bed to study different aspects of ignition designs.[5,6] These surrogates are chosen to best mimic the implosion characteristics of the original design. For example, although ignition designs use an equal mole DT mixture, pure D_2 is commonly used as a surrogate. The different mass densities, however, can cause a difference in implosion dynamics (in particular through the Atwood number, which differs by a factor of 2 at the fuel–shell interface during the deceleration phase[7]).

To explore the effects of fill composition on the implosion dynamics of surrogate fuels, a series of experiments using different ratios of D_2 and ^{3}He was performed. Evaluation of surrogate materials is best done when the materials are chosen to be as nearly hydrodynamically equivalent as possible. D and ^{3}He have a special property in which they have the same value of $(1 + Z)/A$, allowing mixtures of D_2 and ^{3}He to be chosen such that the mass density and the total particle density upon full ionization are identical. This results in the same Atwood number (affecting hydrodynamic instabilities[2,7]) and the same equation of state (EOS).

An additional advantage of these surrogate targets is that products from the D-D nuclear reaction can be measured for all mixtures, whereas measuring the D-D products from a DT implosion has proven difficult for ignition-relevant implosions because of the large background of D-T neutrons. A final advantage of D_2 and ^{3}He mixtures is their emission of D-^{3}He protons that have been extensively used to diagnose ICF implosions on OMEGA.[8–10] **Experimental Setup** (p. 90) is a description of the setup and diagnostics used in the experiments. **Expected Scaling** (p. 92) describes the yield scaling expected of hydrodynamically equivalent implosions. **Experimental Observations** (p. 93) describes the results observed in the experiments as well as comparisons to the expected scaling and 1-D radiation-hydrodynamic simulations. The **Discussion** (p. 97) details possible explanations, and a **Summary** is given on p. 99.

Experimental Setup

Direct-drive implosions were conducted on OMEGA,[11] with 60 beams of frequency-tripled (351-nm) UV light in a 1-ns square pulse and a total energy of 23 kJ. SG4 phase plates[12] and 2-D, 1-THz bandwidth smoothing by spectral dispersion of the laser beam were used;[13] the beam-to-beam energy imbalance was typically between 2% and 4% rms. The spherical targets were CH-shell capsules with diameters between 860 μm and 880 μm; a wall thickness of 15, 20, 24, or 27 μm; and a flash coating of about 0.1-μm aluminum.

The gaseous fill of the capsules was composed of mixtures of D_2 and ^{3}He such that the atomic composition varied from pure D to nearly pure ^{3}He. Two classes of fill pressure were used, low (equivalent to 3-atm D_2) and high (equivalent to 15-atm D_2), with predicted convergence ratios of 37 and 14, respectively. The mixtures within each class are considered hydrodynamically equivalent in that they have the same mass density (and therefore the same Atwood number during the deceleration phase) and, upon full ionization (above a few electron volts), the same total particle density and EOS (ideal monatomic).

Capsule fills are hydrodynamically equivalent if the fill pressures of D_2 (X atm) and ^{3}He (W atm) are chosen to obey

$$X = \frac{3}{4}W = X_0, \tag{1}$$

where X_0 is the hydrodynamically equivalent pure-D_2 fill pressure, which is equal to either 3 atm or 15 atm in this article. The deuterium ion fraction by atom f_D scales with X and X_0 as

$$f_D = \frac{3X}{X + 2X_0}. \quad (2)$$

Since there are only two components to the fill gas, $f_{^3He} = 1 - f_D$.

Two standard gas mixtures were used to fill targets of all types: pure D_2 ($f_D = 1.0$) and a D_2-^{3}He mixture with a 1:1 atomic ratio ($f_D = 0.5$). A series of shots with different mixtures of D_2 and ^{3}He was undertaken for the 20- and 24-μm-thick, high-pressure capsules. In addition to the premixed $f_D = 1.0$ and 0.5 compositions, compositions with $f_D = 0.07$, 0.27, and 0.78 were used.[14]

The error in the fill composition for the "standard" ($f_D = 0.5$) D_2-^{3}He mixture is about 1% of f_D, since it comes premixed. Fill composition errors for the other composition ratios, which must be mixed to order, are also small—less than 3% (Ref. 15) of f_D. This error estimate includes uncertainties in the original fill pressure as well as uncertainties in the leak rates of D_2 and ^{3}He through the storage cell and through the target shell as it is handled before shot time. The total fill pressure is known to better than 10% and is independent of the fill composition.[15]

The following primary nuclear reactions occur in implosions of targets filled with mixtures of D_2 and ^{3}He:

$$\begin{aligned} D + D &\rightarrow {}^3He + n(2.45\ MeV), \\ D + D &\rightarrow T + p(3.0\ MeV), \\ D + {}^3He &\rightarrow {}^4He + p(14.7\ MeV), \end{aligned} \quad (3)$$

where the number in parentheses is the mean birth energy of the second product. Figure 106.26 shows the temperature dependence of the thermal reactivities of the D-^{3}He reaction and the n branch of the D-D reaction, as determined by Bosch and Hale.[16] The branching probability of the n and p branches of the D-D reaction are nearly equal over the temperatures of interest.

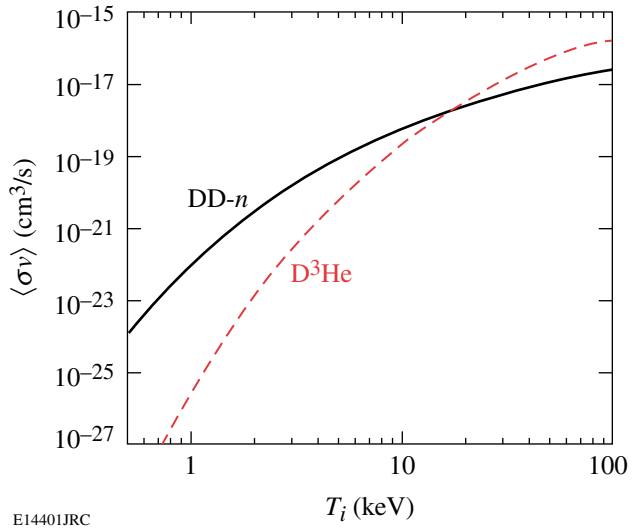

Figure 106.26
DD-n and D^{3}He thermal reactivities as a function of ion temperature.

The principle diagnostics for this work were neutron time-of-flight (nTOF) scintillators[17] to measure the neutron branch of the D-D reaction and multiple wedged-range-filter (WRF) proton spectrometers[8] to measure the protons from the D-^{3}He reaction. The nTOF detectors measure neutron yield and DD burn-averaged ion temperature determined from the Doppler broadening of the neutron signal.

The WRF spectrometers measure the D^{3}He proton spectrum with high resolution (~100 keV). Transient magnetic fields[18] in the implosion corona can redistribute the initially isotropic proton flux emitted by the capsule by 20% rms (typical).[8] The average of the multiple (2 to 7) spectrometers is used to obtain an estimate of the total yield. The mean downshift of the D^{3}He protons from their birth energy of 14.7 MeV is used to infer the areal density (ρR) of the imploded capsule averaged over the D^{3}He proton production.[8]

An alternative measurement of the burn-averaged ion temperature is given by the "ratio method."[19] The ratio of primary yields can be used to infer the ion temperature using the thermal reactivities (Fig. 106.26) and the fuel composition. The ratio of DD-n to D^{3}He reactivities changes by more than three decades from 1 keV to 10 keV, giving a determination of temperature that is not highly sensitive to the exact yields. Differences in burn duration or burn volume of the two constituent reactions result in only minor corrections to the inferred temperature (for example, see the very similar burn histories for DD-n and D^{3}He compression in Fig. 106.27). This correction is small mainly because both reactions are dominated by the high-temperature region near the center.

Temporal diagnostics of the nuclear products include the neutron temporal diagnostic (NTD)[20] for measuring the DD-n burn history and the proton temporal diagnostic (PTD) for measuring the D^{3}He burn history.[21,9] The D^{3}He burn history typically exhibits two periods of proton emission:[22] The first is the "shock burn," which occurs after the first convergence of the shock, near the end of the coasting phase, and before the capsule has fully compressed. About 300 ps later is the "compression burn" (see Fig. 106.27), which occurs during the deceleration and stagnation phases. Spectral measurements of the emitted D^{3}He protons from such capsules can often be decomposed into such "shock" and "compression" components because of the different areal densities they pass through while escaping the capsule (~10 mg/cm^2

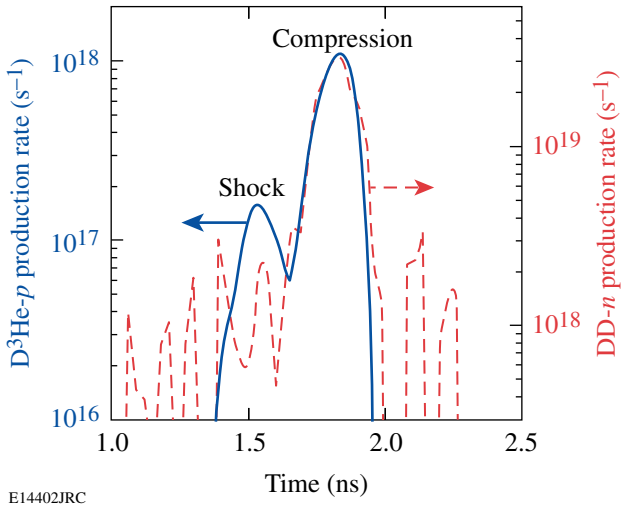

Figure 106.27
Measured D-^{3}He proton (solid) and DD-n (dashed) nuclear production histories of a 24-μm-thick CH shell filled with 6 atm of D_2 and 12 atm of ^{3}He (shot 38525). Distinct shock and compression components are seen in the D-^{3}He production history, whereas there is no evidence of neutrons at shock time in the DD-n production history. The noise level in the burn histories is about 10^{18}/s for DD-n and less than 10^{16}/s for D^{3}He.

at shock and ~60 mg/cm^2 during compression). Because of the much weaker temperature dependence of the DD-n reactivity, the contribution of the high-temperature, low-density shock burn phase to the total yield is much lower than for D^{3}He (typically 0.5% to 1% rather than 5% to 20%).

One-dimensional radiation-hydrodynamic simulations of these implosions were done using the code *LILAC*[23] with a flux limiter of 0.06. Composition scaling simulations were run by changing the initial fill composition while using the same target and laser conditions. To obtain yields of both reactions using compositions of $f_D = 0.0$ and 1.0, the results of those simulations were post-processed as having a trace of the minority species.

Expected Scaling

The nuclear yield is the spatial and temporal integral of the product of reactant densities times the temperature-dependent thermal reactivity of the nuclear reaction under consideration;

$$Y_n = \int \frac{1}{2} n_D^2(\vec{r},t)\langle\sigma v\rangle_{DD-n} d^3\vec{r}dt,$$
$$Y_p = \int n_D(\vec{r},t) n_{^3He}(\vec{r},t)\langle\sigma v\rangle_{D^3He} d^3\vec{r}dt, \quad (4)$$

where Y_n and Y_p are the D-D neutron and D-^{3}He proton yields, n_D and $n_{^3He}$ are the number densities of D and ^{3}He, and $\langle\sigma v\rangle$ is the local thermal reactivity averaged over a Maxwellian ion velocity distribution with temperature T_i. The particle densities and ion temperature will, in general, be functions of position and time. The factor of 0.5 in the DD-n yield accounts for the double-counting of identical reactants.

For the hydrodynamically equivalent mixtures of D_2 and ^{3}He considered here and using the relation $n_i = \rho/Am_p = \rho/(3 - f_D)m_p$, the yields can be re-expressed in terms of f_D;

$$Y_n = \frac{f_D^2}{(3-f_D)^2}\int \frac{\rho^2(\vec{r},t)}{2m_p^2}\langle\sigma v\rangle_{DD-n} d^3\vec{r}dt,$$
$$Y_p = \frac{f_D(1-f_D)}{(3-f_D)^2}\int \frac{\rho^2(\vec{r},t)}{m_p^2}\langle\sigma v\rangle_{D^3He} d^3\vec{r}dt, \quad (5)$$

where m_p is the proton mass and ρ is the mass density. The factor $(3 - f_D)^2$ is equal to A^2 and adjusts for the slightly different ion number densities of D_2 and ^{3}He plasmas at equal mass density. The advantage of this form is that the dependence on the fill composition that determines the difference between hydrodynamically equivalent targets is taken out of the integral.

Figure 106.28 shows the predicted scaling of the D-D neutron and D-^{3}He proton yields as a function of fill composition for hydrodynamically equivalent fuels. Although the character of the composition scaling is very different for the different nuclear

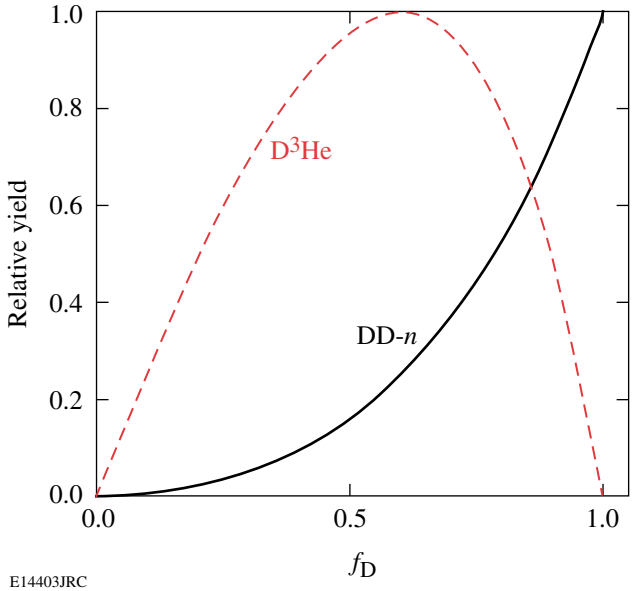

Figure 106.28
Yield dependence of the DD-n and D^{3}He reactions on the D fraction by atom (f_D).

reactions, both curves are independent of the implosion dynamics, so the composition contribution to the yield can be factored out.

All subsequent yields in this article will be scaled according to Eq. (6) unless otherwise noted;

$$\tilde{Y}_n = Y_n \frac{(3 - f_D)^2}{f_D^2}, \qquad \tilde{Y}_p = Y_p \frac{(3 - f_D)^2}{f_D(1 - f_D)}, \tag{6}$$

where $\tilde{Y}_n$ and $\tilde{Y}_p$ denote the scaled DD-*n* and D^3He yields, respectively.

Experimental Observations

The hydrodynamic equivalence of D_2 and ^3He mixtures is most clearly demonstrated by measurements of implosion timing. The time of peak neutron emission (DD-*n* bang time) as well as the duration of the neutron emission (characterized by the full width at half maximum as measured by the NTD) are independent of f_D. In addition, the time of peak proton emission during the compression phase (D^3He compression bang time) and the duration of proton emission (characterized by the FWHM of the compression peak as measured by PTD) are also independent of f_D. Figure 106.29 plots the bang time and burn duration of both nuclear products as a function of f_D for both 20- and 24-μm-thick CH shells. Bang times and burn durations of the two nuclear products are also in good agreement with each other, an example of which can be seen fully in Fig. 106.27.

The measured yield of these hydrodynamically equivalent implosions deviates from the anticipated scaling shown in Fig. 106.28. The deviation of the scaled DD-*n* and D^3He compression yields ($\tilde{Y}_n$ and $\tilde{Y}_{p-c}$) for 20- and 24-μm CH shells with high-pressure fills is shown in Fig. 106.30. The yields have been scaled to the fill composition according to Eq. (6) and, in addition, have been normalized to the yield at $f_D = 0.5$ to emphasize the composition scaling for different measurements. Yields from targets with D-rich and ^3He-rich fuels are typically twice as high as yields from targets with $f_D = 0.5$. This trend is seen for both DD-*n* and D^3He yields and for both 20- and 24-μm shells.[24]

This observed deviation is not seen in 1-D simulations (dashed line in Fig. 106.30), which instead more nearly follows the hydrodynamically equivalent scaling with only minor deviations. Table 106.VIII shows the absolute yields of the normalization points at $f_D = 0.5$ as observed experimentally and as calculated by *LILAC* as well as the absolute DD-*n* yield at $f_D = 1.0$. The DD-*n* experimental yield over calculated yield (YOC) is 21% for $f_D = 0.5$ and 42% or 48% for $f_D = 1.0$.

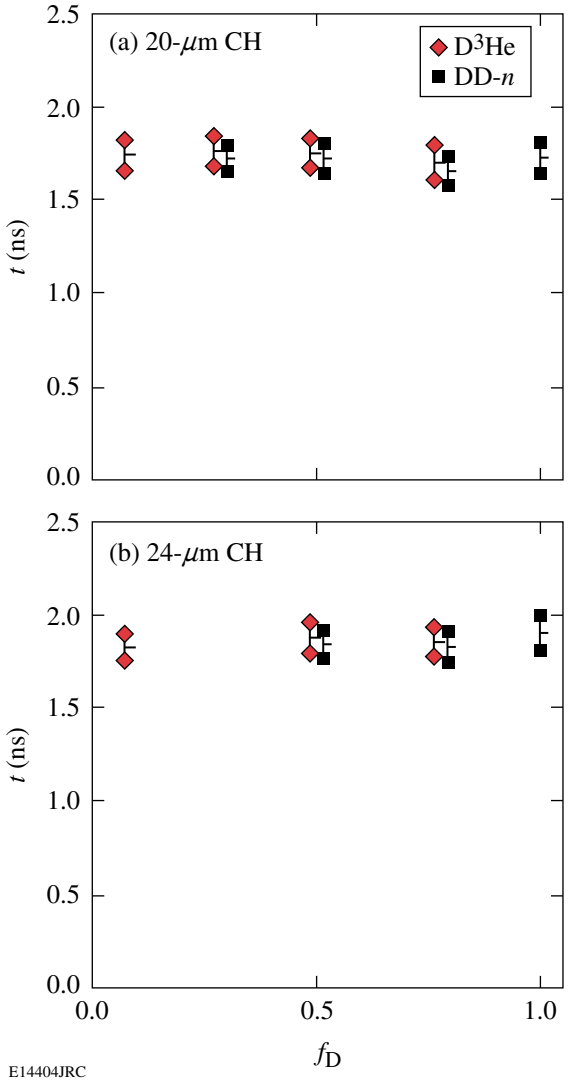

Figure 106.29
Nuclear bang time and burn duration as a function of fill composition for implosions with (a) 20 μm and (b) 24 μm of CH. Open diamonds and solid squares are the times of the half maximum of the peak emission of the D-^3He protons and DD-neutrons, respectively.

A comparison of the YOC for DD-*n* and D^3He on shots with $f_D = 0.5$ illustrates the utility of simultaneous measurement of two nuclear reactions. As shown in Table 106.VIII, the D^3He compression YOC is about 35% compared to the DD-*n* YOC of 21%. The difference in the YOC's for the two nuclear reactions is due to their probing the deviation between the simulated and actual implosion in different ways as a result of their different temperature sensitivities.

Table 106.VIII: Absolute (unscaled) compression yields of DD-n for f_D = 1.0 and 0.5 shots and D^3He for f_D = 0.5 shots as observed experimentally and as calculated by *LILAC*. The experimental yield over calculated yield (YOC) is also shown.

		f_D = 1.0	f_D = 0.5	
Shell	Type	Y_n ($\times 10^{10}$)	Y_n ($\times 10^{10}$)	Y_{p-c} ($\times 10^{8}$)
20-μm CH	Observed	18.7	1.29	6.28
20-μm CH	Calculated	44.6	6.29	18.4
20-μm CH	YOC	42.0%	20.5%	34.1%
24-μm CH	Observed	9.0	0.58	1.46
24-μm CH	Calculated	18.7	2.80	4.22
24-μm CH	YOC	48.1%	20.7%	34.6%

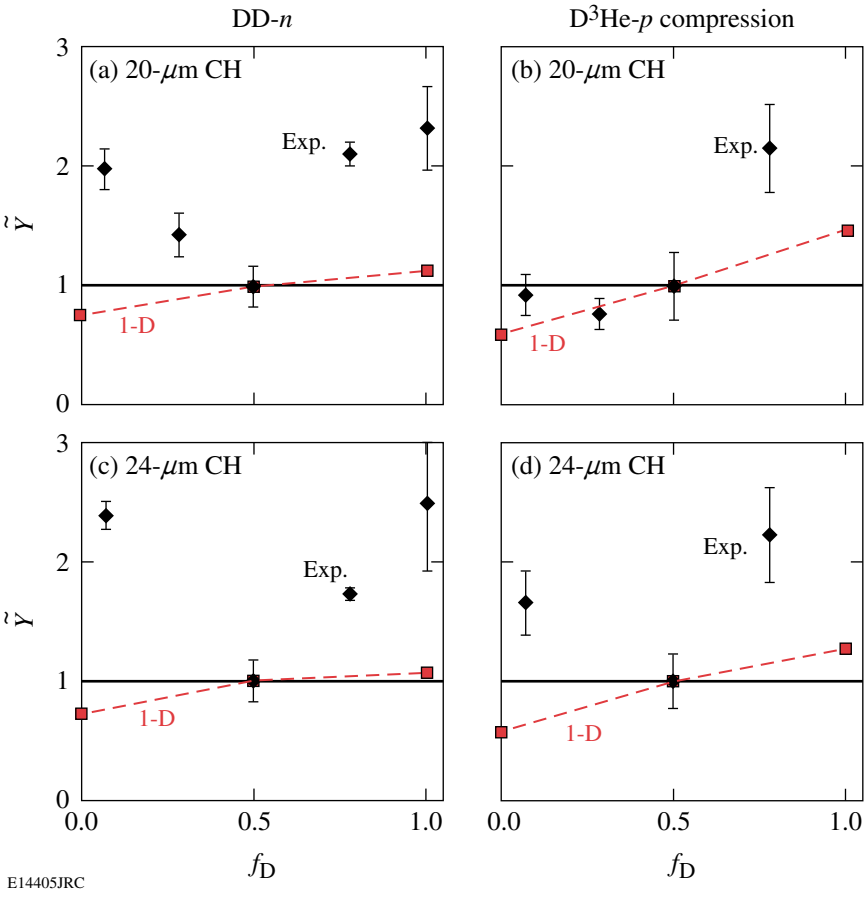

Figure 106.30
Scaled DD-n and D^3He compression yields for high-pressure (X_0 = 15 atm) fills of shells with 20 and 24 μm of CH. (a) $\tilde{Y}_n$, 20 μm; (b) $\tilde{Y}_{p-c}$, 20 μm; (c) $\tilde{Y}_n$, 24 μm; (d) $\tilde{Y}_{p-c}$, 24 μm. All yields have been scaled to fill composition according to Eq. (6) and normalized to the yields at f_D = 0.5. True hydrodynamically equivalent implosions would scale to the same yield (solid line). 1-D simulations with *LILAC* (open squares, dashed line) deviate slightly from hydrodynamic equivalence but not nearly as much as experimental measurements (solid diamonds). The diamonds are the average yield and standard deviation from similar capsules. The 20-μm plots show data reduced from a total of 42 shots, and the 24-μm plots show data reduced from a total of 24 shots.

The "factor of 2" deviation of the yield scaling seen in these 20- and 24-μm CH shell, high-pressure composition campaigns has also been seen over a diverse set of target configurations. Targets with 15-, 20-, 24-, and 27-μm-thick CH shells and with both high and low fill pressures were filled with the two standard compositions; $f_D = 1.0$ and 0.5. Implosions of targets with both composition types emit DD-neutrons, and therefore a comparison of $\tilde{Y}_n$ for like implosions with different compositions was done. Figure 106.31 shows the ratio of scaled yields $\tilde{Y}_n(f_D = 1.0)/\tilde{Y}_n(f_D = 0.5)$ for these implosions. The points at 15 atm and at 20 and 24 μm are the same as the points at $f_D = 1.0$ in Figs. 106.30(a) and 106.30(c). Data reduced from 118 shots predominantly gives a ratio greater than two where a ratio of 1 is anticipated for all capsule types.

The observed ion temperatures are not sufficient to explain the observed yield deviation. The mean ion temperature was measured using two methods: nTOF Doppler broadening and the yield ratio method. The nTOF does not show a trend in the ion temperature, whereas the ion temperature from the ratio method suggests increasing temperatures for higher D content fuels (see Fig. 106.32). Post-processing of 1-D *LILAC* simulations gives burn-averaged temperatures that are not strongly dependent on fill composition. Areal density measurements

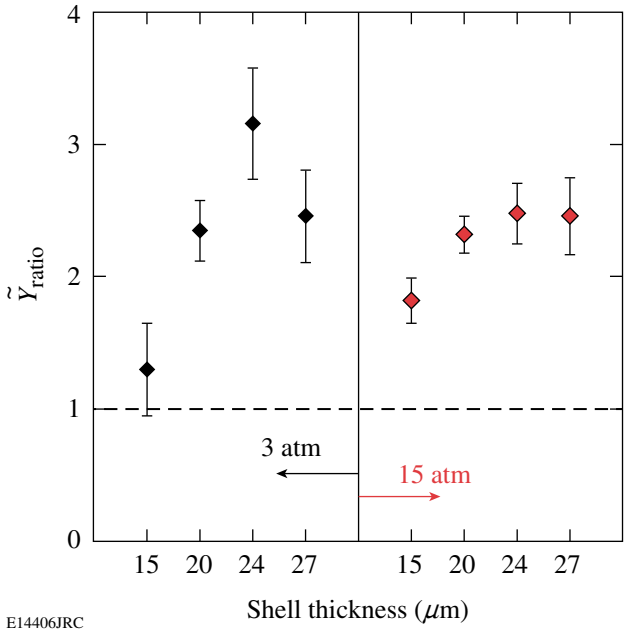

Figure 106.31
The ratio of measured $\tilde{Y}_n$ for $f_D = 1.0$ shots over $\tilde{Y}_n$ for $f_D = 0.5$ shots. The ratio anticipated by the scaling in Fig. 106.28 is 1 (horizontal dashed line) for all target parameters. The points are the ratio of scaled average yields, and the errors are the quadrature sum of the standard deviations of the mean of the two fill compositions. The plot shows data reduced from 118 shots.

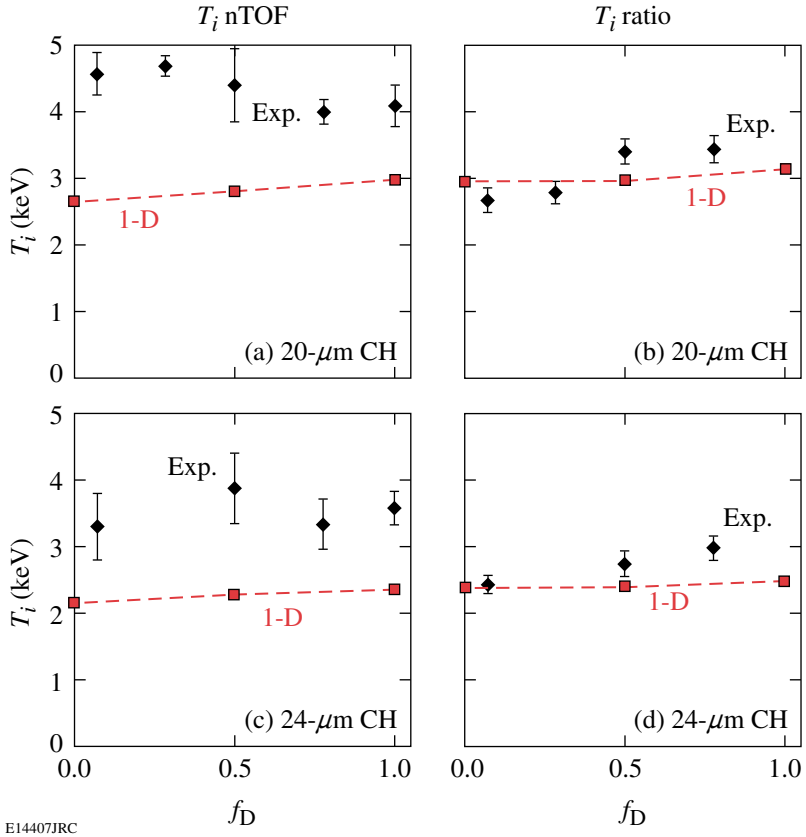

Figure 106.32
Ion temperature as a function of fill composition, as determined by the nTOF for high-pressure fills of (a) 20-μm and (c) 24-μm shells and using the ratio method for (b) 20 μm and (d) 24 μm. The diamonds are the average and standard deviation of experimental observations. The squares and dashed lines are 1-D *LILAC*.

using the downshift of primary D^3He protons (D-^{3}He fuels) or secondary D^3He protons (pure D_2 fuel) show a lower value at compression time for $f_D = 0.5$ (for 24-μm shells, Fig. 106.33), suggesting slightly less compression for those shots.

A similar deviation from the anticipated scaling is also seen for the D^3He shock yield $(\tilde{Y}_{p-s})$, which is emitted about 300 ps earlier than the compression yield and is produced under very different conditions before the start of the deceleration phase and the onset of turbulent mixing[22] at temperatures twice as high as that at compression time and at mass densities less than 10% of those at compression time. Figure 106.34 shows the scaled D^3He shock yield and the shock-yield-averaged ρR for implosions with 24-μm CH shells. The results at shock time are reminiscent of the results at compression time with a lower scaled yield and ρR for the $f_D = 0.5$ shots than for D-rich or ^{3}He-rich mixtures.

A summary of results from figures in this section is listed in Table 106.IX for different mixtures of high-pressure fills in shells with 20 and 24 μm of CH.

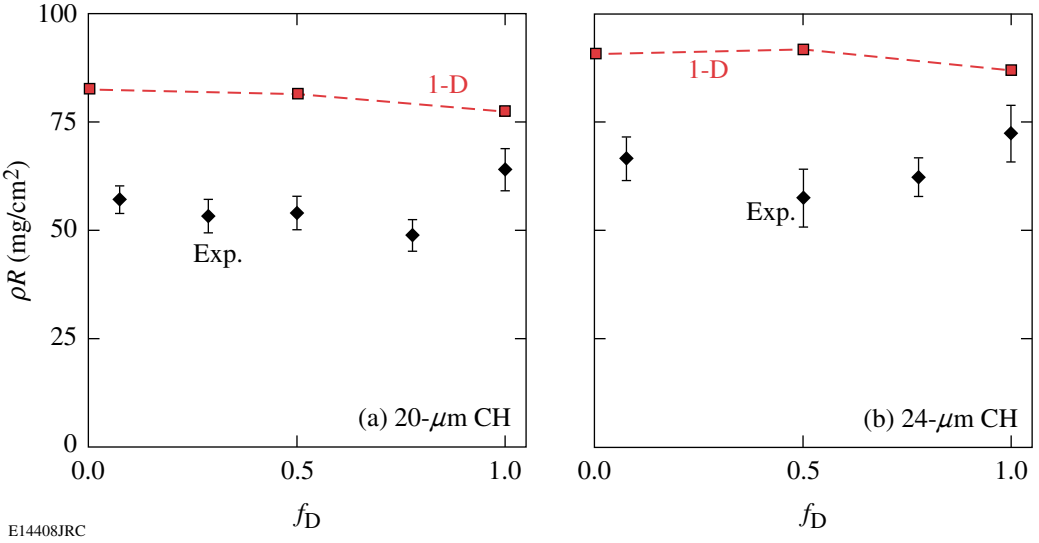

Figure 106.33
Inferred compression burn averaged ρR as a function of fill composition for high-pressure fills of (a) 20-μm-thick and (b) 24-μm-thick shells. The diamonds are the average and standard deviation of experimental observations. The squares and dotted lines are 1-D *LILAC*. For each plot, the higher ρR corresponds to more compression since all targets started with the same shell thickness.

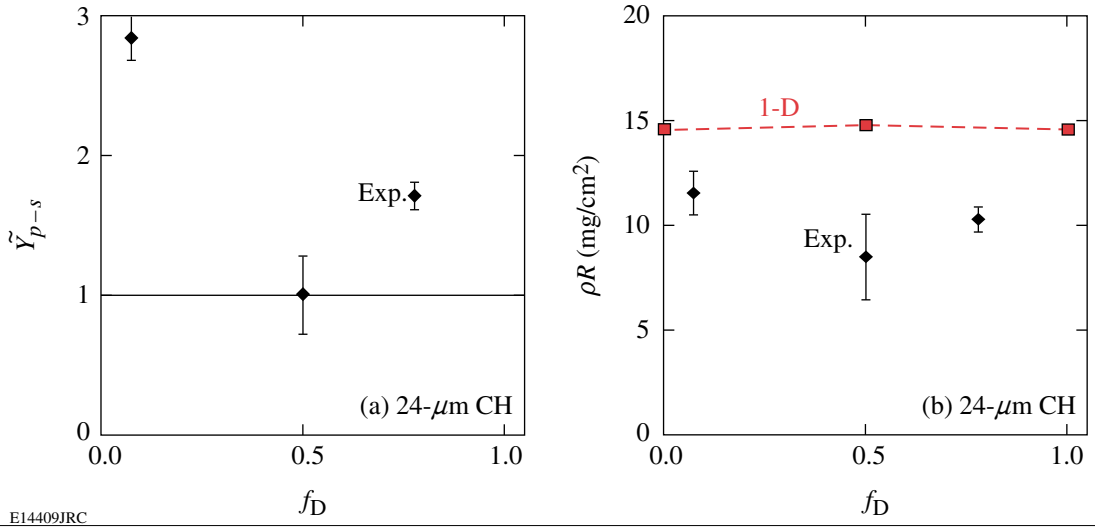

Figure 106.34
D^3He shock results for 24-μm CH capsules. (a) Scaled shock yield and (b) shock-yield-averaged ρR as a function of fill composition. The solid line is hydrodynamically equivalent scaling. The squares and dotted line are 1-D *LILAC*. Diamonds are the average and standard error of experimental observations.

Table 106.IX: D fraction by atom, number of shots averaged, DD-n, D^3He compression and shock yields (scaled by fill composition and normalized to $f_D = 0.5$), ion temperature, areal density, and DD bang time for high-pressure fills for two different shell thicknesses.

Shell	f_D	Number of shots	$\lvert\tilde{Y}_n\rvert$	$\lvert\tilde{Y}_{p-c}\rvert$	$\lvert\tilde{Y}_{p-s}\rvert$	T_i nTOF (keV)	T_i ratio (keV)	ρR (mg/cm^2)	t_{bang} (ns)
CH[20]	1.00	22	2.32	–	–	4.1	–	64	1.73
CH[20]	0.78	5	2.10	2.15	0.77	4.0	3.4	49	1.65
CH[20]	0.50	8	1.00	1.00	1.00	4.4	3.4	54	1.72
CH[20]	0.28	4	1.43	0.77	0.85	4.7	2.8	53	1.73
CH[20]	0.07	3	1.98	0.93	1.23	4.6	2.7	57	–
CH[24]	1.00	10	2.48	–	–	3.6	–	72	1.91
CH[24]	0.78	2	1.73	2.22	1.71	3.3	3.0	62	1.83
CH[24]	0.50	9	1.00	1.00	1.00	3.9	2.7	58	1.87
CH[24]	0.07	3	2.38	1.65	2.84	3.3	2.4	64	–

Discussion

A closer look at the possibility of a measurement error is certainly warranted when observations deviate so far from the scaling derived from simple principles as well as from computer simulations. The individual measurement error on a given shot is about 10% for both DD-n and D^3He yields; however, the shot-to-shot yield variation for nominally identical shots is closer to 20% rms. Averaging the results from many like shots reduces the standard deviation of the mean considerably, in most cases below 10%. Systematic yield uncertainties in the diagnostics are unlikely to cause the yield scaling. The yield measurements for the two nuclear reactions use different diagnostics, using different principles, yet measured the same deviation.

The deviation in the yield scaling from Eq. (4) must then be explained through the differences in composition, temperature, density, burn volume, or burn duration of the target during the implosion. According to temporal measurements of nuclear burn histories, the implosion timing does not depend on the fill composition. Uncertainty in the composition is at most a couple of percent, which is not enough to affect the yields by a factor of 2. In addition, composition errors affect the DD-n and D^3He yield scaling in different ways (Fig. 106.28), yet the same deviation is seen for both.

The observed trend of the ratio-inferred ion temperature could be part of the story because of the strong dependence of the thermal reactivities of both reactions at the temperatures of interest. The DD-n and D^3He reactivities scale approximately as T_i^4 and T_i^7 near $T_i = 3$ keV. A linear fit through the observed ratio-inferred T_i in Fig. 106.32(d) was used to adjust the hydrodynamically equivalent $\tilde{Y}_n$ scaling. The solid curve in Fig. 106.35(a) plots this T_i ratio yield scaling against the observed yields from Fig. 106.30(c). This corrected scaling looks better for D-rich fuels but deviates further than the uncorrected hydrodynamically equivalent scaling from the observed yields for ^3He-rich fuels. Since there was no clear trend in the nTOF-derived temperatures, a similar yield scaling fit was not done using the nTOF temperatures.

The two remaining factors of fuel density and burn volume are related to the compression of the capsule, which can be inferred by measurements of ρR. A simple model of the implosion that assumes that the shell temperature and shell aspect ratio at bang time does not depend on fill composition determines that the yield scales approximately as $(\rho R)^3$. The open circles in Fig. 106.35(b) plot this ρR yield scaling against the observed yields from Fig. 106.30(c). Higher ρR's were observed for high and low D concentrations compared to the 50/50 mixture. The shape predicted from the $(\rho R)^3$ scaling is in qualitative agreement with the measurements, though it does not show quite as strong a scaling.

Although additional measurements suggest that some combination of ion temperature and density might be sufficient to explain the observed yield deviation, these factors must come from some physical mechanism, a number of which will be explored below.

The deviation from the assumed hydrodynamic equivalence is unlikely to be explained by 2-D or 3-D hydrodynamic effects, including hydrodynamic instabilities and turbulent mixing that

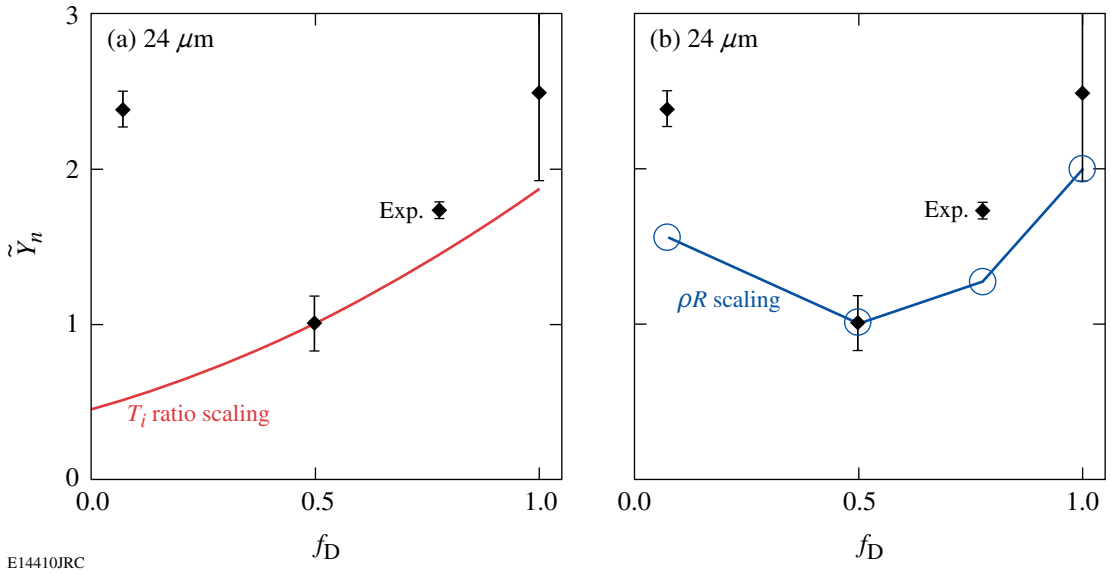

Figure 106.35
Measured (solid diamonds) DD-n yields as a function of f_D for 24-μm shells with high pressure from Fig. 106.30(c). In these plots, the hydrodynamically equivalent scaling has been adjusted to take into account the effects of measured ion temperature and areal density on the yield. (a) The solid line is a T_i-corrected scaling curve, based on a linear fit to the experimental T_i ratios in Fig. 106.32(d). (b) The open circles and connecting line include a ρR correction based on the measured ρR values shown in Fig. 106.33(b).

would reduce the burn volume and truncate the burn duration. A similar trend was experimentally observed over a wide range of physical situations in which 2-D hydrodynamic effects would likely have behaved very differently. Implosions with thicker shells are considered to be more hydrodynamically stable,[25] yet the same yield trend is seen for 20- and 24-μm shells with a high fill pressure. Implosions with a low fill pressure are considered less hydrodynamically stable, yet the yield trend is the same as for the high fill pressure (Fig. 106.31). A similar trend is also seen for D^{3}He shock burn measurements, despite the fact that it has been shown that there is no atomic-level mixing in the burn region at shock time.[22] Thus, pure hydrodynamics cannot explain the observed differences.

A wealth of data seems to exclude pure hydrodynamic differences between these mixtures as the mechanism for the observed variation in their yields (as it should be since they were chosen to be hydrodynamically equivalent). The deviation from hydrodynamic equivalence is likely to be due to the microscopic details of the mixture. It may have something to do with the variation in the average Z in the fuel, which varies from 1 (pure D_2) to nearly 2 (^{3}He rich), the difference in ion masses or a subtlety in the statistical treatment of mixtures.

Bremsstrahlung radiation scales as $\sim \rho^2 T_e^{1/2} Z^3 / A^2$, which for these mixtures differs by a factor of 3.6 from pure D_2 (low) to pure ^{3}He, assuming the same density and temperature. A factor of 3 difference in the radiated power may then trigger differences in the absorption in the CH and initiate changes in the implosion dynamics. However, the yield discrepancy trend is about the same for cases with significantly different radiative properties, such as for low-pressure and high-pressure fills as well as at both shock and compression time. The difference in density in these scenarios radically affects the efficiency of bremsstrahlung radiation. In addition, the yield deviation is not monotonic with the D fraction, so bremsstrahlung radiation seems unlikely as the sole mechanism.

Thermal conduction in these dynamic implosions can be difficult to calculate because of nonequilibrium conditions and other nonlocal effects. To get a sense of the scaling, however, consider the Spitzer–Harm electron thermal conduction[26]

$$q_{SH} = -K \nabla T,$$

$$K \propto \delta(Z) \frac{T_e^{5/2}}{Z m_e^{1/2} \ln \Lambda},$$

$$\delta(Z) = \frac{Z + 0.24}{Z + 0.42}. \tag{7}$$

Ignoring the Coulomb logarithm variation, pure D_2 has a 32% higher classical conductivity than pure ^{3}He and is 17% higher than the standard D_2-^{3}He mixture (using "average" ions). Ion thermal conduction has a similar form, but with a much stronger Z dependence.[27] Ion conduction is relatively small when the ion and electron temperatures are equal but can become important when the ion temperature is higher, such as for shock heating. But for both types of thermal conduction, the trend is again monotonic with a D fraction.

Shock heating initially puts most energy into heating the ions, with more energy going to heavier ions.[28] Equal-density mixtures of D_2 and ^{3}He will absorb the same total amount of energy from a shock front, but mixtures with a higher concentration of ^{3}He will have a higher initial ion temperature due to the higher average ion mass (and corresponding lower ion density). A slight difference in this initial state of the gas might, after compression, be enough to change the dynamics and the resulting nuclear yields. The compression condition will be quite a bit different for the different implosion types (high and low pressure, thin and thick shells), yet the same deviation is seen in many cases. It is also difficult to explain the nonmonotonic trend with this picture.

It is possible that there is stratification of the ion species during the deceleration phase. The scaled performance of the "pure" fuels seems to be greatest, so perhaps the mixture of different species is important. During the deceleration phase, the ^{3}He concentration might be slightly enhanced near the center. The hot center will then have a lower nuclear yield due to scarcer D ions. In this picture, though, the ^{3}He-rich fuels should also have a reduced yield, so the nonmonotonic trend is again a problem.

The plausibility of stratification can be considered using simple arguments. Because of the high density during the compression phase, any concentration enhancement will have to come through a difference in diffusion of the D and ^{3}He ions. With plasma parameters typical of the fill early in the compression burn (4 keV, 3 g/cc), it is found that the time it takes even one particle to diffuse across the capsule is very much longer than the implosion time.

Kinetic effects could play an important role in the observed yield scaling. A non-Maxwellian velocity distribution could significantly alter nuclear production, particularly at the time of shock collapse, where the distribution is far from Maxwellian. It has also been suggested that yield degradation could result from the loss of ions in the tail of the distribution, which normally dominate the nuclear production. The longer mean free paths of the ions in the tail may allow them to escape the fuel region if the $\rho R < 10$ mg/cm^2 (Ref. 29). It is not sufficient, though, that kinetic effects only change the nuclear production; a kinetic effect must change the nuclear production nonmonotonically with the D fraction and by a factor of 2 between pure and mixed D and ^{3}He.

Many processes used to explain the observed yield scaling have been considered here but no single mechanism is sufficient to explain the trend.

Summary

In summary, experimental observations of the scaling of nuclear yields from implosions with hydrodynamically equivalent mixtures of D_2 and ^{3}He deviate from the scaling determined using a simple consideration of composition ratios as well as from a scaling based on 1-D radiation-hydrodynamic simulations. This deviation is particularly puzzling since the trend is not monotonic with the D fraction; the scaled D^{3}He yield is lower than the scaled yields on both the D_2-rich and ^{3}He-rich sides.

The same scaling deviation is observed in diverse physical situations, including implosions of targets with initial fill pressures of 3 and 15 atm and target shell thicknesses of 15, 20, 24, and 27 μm of CH. A similar yield scaling deviation is observed for both DD-n and D^{3}He yields despite the drastically different dependence of their yields on composition and temperature. Overall, a similar scaling deviation is seen for both the shock and compression components of the D^{3}He yield, corresponding to times separated by several hundred picoseconds and reflecting very different plasma conditions.

It has been shown that measurements of the burn-averaged ion temperature, using two different methods, are insufficient to explain the entire yield scaling deviation. Errors in the initial fill composition of the D_2 and ^{3}He mixtures and differences in the implosion timing have also been excluded. Measurements of the burn-averaged areal density ρR suggest that D_2 and ^{3}He mixtures with a f_D near 0.5 might experience less compression, resulting in a lower yield.

A number of possible mechanisms that may cause the scaling are considered, but no dominant mechanism has been identified. Differences in the radiative and transport properties of different D_2 and ^{3}He mixtures are included in 1-D simulations, but apparently do not have as great an effect on the yield as what was observed. Hydrodynamic instabilities in 2-D and

3-D appear to be ruled out. The initial gas state set by the converging shock, ion species stratification, and kinetic effects were also considered.

This study raises some concern as to the near equivalence of D_2 as a DT fuel surrogate for studying implosion dynamics. Even when the mass density of the D_2 and ^{3}He mixtures is the same, we see discrepancies in the yield although it is not clear what mechanism causes the discrepancy and whether it is due to a difference in the average Z, ion masses, or transport properties of mixed materials. To explore such issues, further scrutiny of the ion conductivity and its effects on implosion dynamics is underway, which may be an important factor because of its strong Z dependence.

An investigation of the yield scaling at constant Z could be accomplished by using different fuel mixtures, including mixtures of D and T, and an extension of this study with mixtures of D_2, ^{3}He, and either H_2 or ^{4}He. Experiments are being actively planned that would vary the D and T mixture with the intention of simultaneously measuring the absolute yield of both DT and DD,[30] the results of which will have direct relevance for ignition target fills and will take us a step closer to understanding the present conundrum.

ACKNOWLEDGMENT

The authors express their gratitude to the OMEGA engineers and operations crew who supported these experiments. This work was supported in part by the U.S. Department of Energy Office of Inertial Confinement Fusion (Grant No. DE-FG03-03NA00058), by the Lawrence Livermore National Laboratory (Subcontract No. B543881), and by the Laboratory for Laser Energetics (Subcontract No. 412160-001G) under Cooperative Agreement DE-FC52-92SF19460, University of Rochester, and New York State Energy Research and Development Authority.

REFERENCES

1. J. Nuckolls *et al*., Nature **239**, 139 (1972).
2. J. D. Lindl, *Inertial Confinement Fusion: The Quest for Ignition and Energy Gain Using Indirect Drive* (Springer-Verlag, New York, 1998).
3. S. Atzeni and J. Meyer-ter-Vehn, *The Physics of Inertial Fusion: Beam Plasma Interaction, Hydrodynamics, Hot Dense Matter*, International Series of Monographs on Physics (Clarendon Press, Oxford, 2004).
4. S. E. Bodner, D. G. Colombant, J. H. Gardner, R. H. Lehmberg, S. P. Obenschain, L. Phillips, A. J. Schmitt, J. D. Sethian, R. L. McCrory, W. Seka, C. P. Verdon, J. P. Knauer, B. B. Afeyan, and H. T. Powell, Phys. Plasmas **5**, 1901 (1998).
5. F. J. Marshall, J. A. Delettrez, V. Yu. Glebov, R. P. J. Town, B. Yaakobi, R. L. Kremens, and M. Cable, Phys. Plasmas **7**, 1006 (2000).
6. R. L. McCrory, R. E. Bahr, R. Betti, T. R. Boehly, T. J. B. Collins, R. S. Craxton, J. A. Delettrez, W. R. Donaldson, R. Epstein, J. Frenje, V. Yu. Glebov, V. N. Goncharov, O. Gotchev, R. Q. Gram, D. R. Harding, D. G. Hicks, P. A. Jaanimagi, R. L. Keck, J. Kelly, J. P. Knauer, C. K. Li, S. J. Loucks, L. D. Lund, F. J. Marshall, P. W. McKenty, D. D. Meyerhofer, S. F. B. Morse, R. D. Petrasso, P. B. Radha, S. P. Regan, S. Roberts, F. Séguin, W. Seka, S. Skupsky, V. Smalyuk, C. Sorce, J. M. Soures, C. Stoeckl, R. P. J. Town, M. D. Wittman, B. Yaakobi, and J. D. Zuegel, Nucl. Fusion **41**, 1413 (2001).
7. S. P. Regan, J. A. Delettrez, V. Yu. Glebov, V. N. Goncharov, J. P. Knauer, J. A. Marozas, F. J. Marshall, R. L. McCrory, P. W. McKenty, D. D. Meyerhofer, P. B. Radha, T. C. Sangster, S. Skupsky, V. A. Smalyuk, C. Stoeckl, J. R. Rygg, J. A. Frenje, C. K. Li, R. D. Petrasso, and F. H. Séguin, Bull. Am. Phys. Soc. **50**, 113 (2005).
8. F. H. Séguin, J. A. Frenje, C. K. Li, D. G. Hicks, S. Kurebayashi, J. R. Rygg, B.-E. Schwartz, R. D. Petrasso, S. Roberts, J. M. Soures, D. D. Meyerhofer, T. C. Sangster, J. P. Knauer, C. Sorce, V. Yu. Glebov, C. Stoeckl, T. W. Phillips, R. J. Leeper, K. Fletcher, and S. Padalino, Rev. Sci. Instrum. **74**, 975 (2003).
9. J. A. Frenje, C. K. Li, F. H. Séguin, J. Deciantis, S. Kurebayashi, J. R. Rygg, R. D. Petrasso, J. Delettrez, V. Yu. Glebov, C. Stoeckl, F. J. Marshall, D. D. Meyerhofer, T. C. Sangster, V. A. Smalyuk, and J. M. Soures, Phys. Plasmas **11**, 2798 (2003).
10. F. H. Séguin, J. L. DeCiantis, J. A. Frenje, S. Kurebayashi, C. K. Li, J. R. Rygg, C. Chen, V. Berube, B. E. Schwartz, R. D. Petrasso, V. A. Smalyuk, F. J. Marshall, J. P. Knauer, J. A. Delettrez, P. W. McKenty, D. D. Meyerhofer, S. Roberts, T. C. Sangster, K. Mikaelian, and H. S. Park, Rev. Sci. Instrum. **75**, 3520 (2004).
11. T. R. Boehly, D. L. Brown, R. S. Craxton, R. L. Keck, J. P. Knauer, J. H. Kelly, T. J. Kessler, S. A. Kumpan, S. J. Loucks, S. A. Letzring, F. J. Marshall, R. L. McCrory, S. F. B. Morse, W. Seka, J. M. Soures, and C. P. Verdon, Opt. Commun. **133**, 495 (1997).
12. F. J. Marshall, J. A. Delettrez, R. Epstein, R. Forties, R. L. Keck, J. H. Kelly, P. W. McKenty, S. P. Regan, and L. J. Waxer, Phys. Plasmas **11**, 251 (2004).
13. S. Skupsky and R. S. Craxton, Phys. Plasmas **6**, 2157 (1999).
14. The f_D = 0.78 shots plotted on the 20-μm-CH figures actually had 19-μm-thick shells.
15. M. J. Bonino, Laboratory for Laser Energetics, private communication (2006).
16. H.-S. Bosch and G. M. Hale, Nucl. Fusion **32**, 611 (1992).
17. R. A. Lerche and T. J. Murphy, Rev. Sci. Instrum. **63**, 4880 (1992).
18. Tangential electric fields have not been excluded as the cause for the anisotropic proton emission, but for these implosions there is no radial E field when the protons are emitted.
19. C. K. Li, D. G. Hicks, F. H. Séguin, J. A. Frenje, R. D. Petrasso, J. M. Soures, P. B. Radha, V. Yu. Glebov, C. Stoeckl, D. R. Harding, J. P. Knauer, R. L. Kremens, F. J. Marshall, D. D. Meyerhofer, S. Skupsky, S. Roberts, C. Sorce, T. C. Sangster, T. W. Phillips, M. D. Cable, and R. J. Leeper, Phys. Plasmas **7**, 2578 (2000).
20. R. A. Lerche, D. W. Phillion, and G. L. Tietbohl, Rev. Sci. Instrum. **66**, 933 (1995).

21. C. Stoeckl, V. Yu. Glebov, S. Roberts, T. C. Sangster, R. A. Lerche, R. L. Griffith, and C. Sorce, Rev. Sci. Instrum. **74**, 1713 (2003).

22. R. D. Petrasso, J. A. Frenje, C. K. Li, F. H. Séguin, J. R. Rygg, B. E. Schwartz, S. Kurebayashi, P. B. Radha, C. Stoeckl, J. M. Soures, J. Delettrez, V. Yu. Glebov, D. D. Meyerhofer, and T. C. Sangster, Phys. Rev. Lett. **90**, 095002 (2003).

23. J. Delettrez, R. Epstein, M. C. Richardson, P. A. Jaanimagi, and B. L. Henke, Phys. Rev. A **36**, 3926 (1987).

24. Except for the D^3He yield from ^3He-rich, 20-μm-thick target implosions.

25. S. P. Regan, J. A. Delettrez, V. N. Goncharov, F. J. Marshall, J. M. Soures, V. A. Smalyuk, P. B. Radha, B. Yaakobi, R. Epstein, V. Yu. Glebov, P. A. Jaanimagi, D. D. Meyerhofer, T. C. Sangster, W. Seka, S. Skupsky, C. Stoeckl, D. A. Haynes, Jr., J. A. Frenje, C. K. Li, R. D. Petrasso, and F. H. Séguin, Phys. Rev. Lett. **92**, 185002 (2004).

26. L. Spitzer, Jr. and R. Härm, Phys. Rev. **89**, 977 (1953).

27. S. I. Braginskii, in *Reviews of Plasma Physics*, edited by Acad. M. A. Leontovich (Consultants Bureau, New York, 1965), Vol. 1, p. 205.

28. Ya. B. Zel'dovich and Yu. P. Raizer, *Physics of Shock Waves and High-Temperature Hydrodynamic Phenomena*, edited by W. D. Hayes and R. F. Probstein (Dover Publications, Mineola, NY, 2002).

29. D. B. Henderson, Phys. Rev. Lett. **33**, 1142 (1974).

30. Only recent technological advances have made the detection of DD neutrons in the background of DT neutrons feasible. See V. Yu. Glebov, D. D. Meyerhofer, T. C. Sangster, C. Stoeckl, S. Roberts, C. A. Barrera, J. R. Celeste, L. S. Dauffy, C. J. Cerjan, D. C. Eder, R. L. Griffith, S. W. Haan, B. A. Hammel, S. P. Hatchett, N. Izumi, J. R. Kimbrough, J. A. Koch, O. L. Landen, R. A. Lerche, B. J. MacGowan, M. J. Moran, E. W. Ng, T. W. Phillips, P. M. Song, R. Tommassini, B. K. F. Young, S. E. Caldwell, G. P. Grim, S. C. Evans, L. Disdier, M. Houry, I. Lantuejoul, G. A. Chandler, G. W. Cooper, R. J. Lepeer, R. E. Olson, C. L. Ruiz, M. A. Sweeney, S. P. Padalino, C. Horsfield, and B. A. Davis, "Development of Nuclear Diagnostics for the National Ignition Facility," to be presented at the 16th Topical Conference on High-Temperature Diagnostics, Williamsburg, VA, 7–11 May 2006.